

This article appeared in a journal published by Elsevier. The attached copy is furnished to the author for internal non-commercial research and education use, including for instruction at the authors institution and sharing with colleagues.

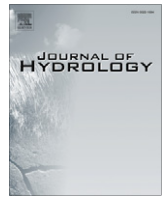
Other uses, including reproduction and distribution, or selling or licensing copies, or posting to personal, institutional or third party websites are prohibited.

In most cases authors are permitted to post their version of the article (e.g. in Word or Tex form) to their personal website or institutional repository. Authors requiring further information regarding Elsevier's archiving and manuscript policies are encouraged to visit:

<http://www.elsevier.com/authorsrights>

Contents lists available at [SciVerse ScienceDirect](http://www.sciencedirect.com)

Journal of Hydrology

journal homepage: www.elsevier.com/locate/jhydrol

3D analysis of geometry and flow changes in a limestone fracture during dissolution

Catherine Noiriel^{a,*}, Philippe Gouze^b, Benoît Madé^c^a Géosciences Environnement Toulouse (GET), Observatoire Midi-Pyrénées, Université Paul Sabatier, CNRS, IRD, 31400 Toulouse, France^b Géosciences Montpellier, UMR 5243, CNRS, Université de Montpellier II, 34095 Montpellier, France^c Agence Nationale pour la gestion des Déchets Radioactifs, 92298 Châtenay Malabry, France

ARTICLE INFO

Article history:

Received 20 July 2012

Received in revised form 5 December 2012

Accepted 26 January 2013

Available online 14 February 2013

This manuscript was handled by Laurent Charlet, Editor-in-Chief, with the assistance of Tamotsu Kozaki, Associate Editor

Keywords:

Fracture

X-ray micro-tomography

Dissolution

CO₂

Limestone

Flow modelling

SUMMARY

The effects of reactive transport on fracture geometry and fluid flow were investigated through an integrated experimental and modelling approach. A fractured limestone sample (90% calcite) was injected with an acidic CO₂-rich solution over a period of 55 h to induce carbonate dissolution. The changes in fracture geometry and related parameters are reported for six data sets obtained from synchrotron X-ray micro-tomography experiments. A series of algorithms was used to extract the aperture and fracture walls from 3D images and allowed quantification of the geometry changes with an optical resolution of 4.91 μm. In addition, measurement of fluid chemistry, hydraulic tests and computation of Navier–Stokes flow constrained the characterisation of the dissolution process. The effects of reactive transport on fracture geometry and fluid flow were then discussed. The presence of silicates in the rocks led to heterogeneous dissolution at the micro-scale, despite dissolution appearing to be quite homogeneous at sample-scale. No formation of preferential flow pathways was noticed, although heterogeneous dissolution at the micro-scale led to fracture walls and aperture decorrelation, and to modification of the flow velocity profiles in the fracture.

© 2013 Elsevier B.V. All rights reserved.

1. Introduction

Fractures control the flow and transport of fluids and pollutants in low-permeability rocks. Assessing long-term transport of contaminants in fractured rocks is essential, especially regarding nuclear waste storage, geothermal energy or CO₂ sequestration in reservoirs. For these situations, long-lasting flow of fluids in disequilibrium with the rock is expected and dissolution (or precipitation) processes can quickly and deeply alter the geometry of fractures, and, as a consequence, their hydraulic and transport properties, such as permeability and dispersivity. For instance, karst formation in limestone is certainly the most remarkable example of alteration of flow and transport properties over a relatively short period of time. It is probable that in many geological and environmental applications, fracture parameters must be considered as variables. Yet, the prediction of flow and transport changes in fractures undergoing chemical reactions is challenging due to the complexity of fluid–rock interactions and the possible triggering of positive (or negative) feedbacks.

Fractures are heterogeneous structures, the macroscopic physical properties of which depend on local characteristics. For

instance, fracture permeability and transport properties are closely related to the microstructure, such as physico-chemical properties and spatial distribution of the rock-forming minerals, fracture wall roughness, tortuosity, and contacting asperities. Aperture distribution and anisotropy are also main parameters in determining the flow and transport properties. Therefore, fracture geometry determination is important to model flow and transport accordingly.

The control of various fracture parameters on fluid flow (Appendix A) and of transport of solutes (Appendix B) into fractures has been discussed extensively. However, discrepancies between numerical models and natural configurations are still expected because numerical models often idealise the fracture geometry or take into account the presence of only one reactive mineral, despite rocks are rarely being mono-mineral. The advent of non-invasive and non-destructive techniques has improved in situ characterisation of fracture geometry (Bertels and DiCarlo, 2001; Keller, 1998; Vandersteen et al., 2003) and flow (Dijk et al., 1999; Karpyn et al., 2007; Kumar et al., 1997), which now appear to be very pertinent for observing changes during dynamic experiments (Detwiler, 2008; Detwiler et al., 2003; Dijk et al., 2002; Ellis et al., 2011; Enzmann et al., 2004; Gouze et al., 2003; Landis et al., 2003; Noiriel et al., 2007a, 2007b). Experimental effort, including direct permeability and geometry measurements, is still required to predict the long-term evolution of such heterogeneous systems.

The present study aims to characterise fracture geometry and flow changes during a flow-through dissolution experiment in a

* Corresponding author. Address: Géosciences Environnement Toulouse (GET), UMR 5533, Université Paul Sabatier, CNRS, IRD, CNES, 14, avenue Edouard Belin, 31400 Toulouse, France. Tel.: +33 561 332 589; fax: +33 561 332 560.

E-mail address: catherine.noiriel@get.obs-mip.fr (C. Noiriel).

slightly argillaceous limestone sample. By developing a technique to measure repetitively the fracture void geometry, a direct comparison can be made between geometrical and hydraulic property changes and the dissolution process. X-ray micro-tomography allowed the collection of the different parameters describing the changes in fracture geometry both before the experiment and after different stages of dissolution. The effects of dissolution on the fracture geometry were characterised after extraction of the two fracture walls and the aperture from 3D image volumes. Measurement of fluid chemistry and permeability complementary constrained the characterisation of the dissolution process. In addition, fluid flow was computed in the fracture and the resulting hydraulic aperture (a_{h-NS}) was compared with three others independent experimental measurements of the fracture aperture, i.e. hydraulic aperture (a_h) determined from hydraulic tests, mechanical aperture (a_m) determined from XMT, and chemical aperture (a_c) determined from mass balance calculation. Finally, the implication of aperture increase and rock mineralogy, flow, transport and geometry changes will be discussed.

2. Experimental procedure

2.1. Sample characteristics

The flow-through experiment was carried out using a slightly argillaceous limestone that contains about 10% of silicate minerals (principally clays, with a minor amount of quartz) and less than 1% of iron oxides. The carbonate matrix is essentially composed of partially recrystallized micro-crystalline calcite and to a minor extent by biogenic fragments crystallised in sparite.

A cylindrical sample of 15 mm in length and 9 mm in diameter was artificially fractured using a Brazilian-like test to produce a longitudinal fracture parallel to the cylinder axis. The two fracture walls were put together and sealed with epoxy resin on their edges to prevent any mechanical displacements of the fracture walls during experiment. The external surface of the fractured sample apart from the fracture inlet and outlet was also covered with epoxy resin to avoid dissolution.

2.2. Flow-through experiment

The inlet fluid used in the experiment was a 0.010 ± 0.001 M NaCl solution prepared from reagent-grade salt diluted in deionised water. The fluid, initially degassed, was maintained at equilibrium with CO_2 at a partial pressure of 0.10 ± 0.01 MPa during the experiment.

After vacuum saturation with deionised water, the sample was injected with the inlet fluid using a dual piston pump at a

controlled flow rate of $100 \text{ cm}^3 \text{ h}^{-1}$ ($2.78 \times 10^{-8} \text{ m}^3 \text{ s}^{-1}$). The confining pressure was equal to the pressure at the sample inlet. The pressure at the outlet was maintained at 0.13 MPa using a calibrated back-pressure controller to avoid CO_2 degassing during the experiment.

Permeability was calculated from the differential pressure record between the sample inlet and outlet (ΔP) using the steady-state flow method (Eq. (A.2)), initially ($t = t_0$) and at the end of each stage of dissolution, i.e. after 8 h (t_1), 16 h (t_2), 28 h (t_3), 37 h (t_4) and 55 h (t_5) from the start of the experiment.

Both the inlet and outlet pH were recorded continuously to detect either potential CO_2 saturation changes of the inlet fluid or variation of the alkalinity of the outlet solution. The outlet solution was also sampled repeatedly for major and minor ions analysis by ICP-AES (inductive coupled plasma-atomic emission spectroscopy). A schematic representation of the flow-through experiment is presented in Fig. 1a.

2.3. Geometry characterisation using synchrotron X-ray micro-tomography

2.3.1. X-ray tomography imaging of the fracture

The geometry of the fracture was obtained after processing of the XMT data sets acquired at the European Synchrotron Radiation Facility ID19 beam-line (Grenoble, France). A total of six data sets were collected at times t_0 to t_5 . The XMT method provides non-invasive and non-destructive visualisation and characterisation of the 3D sample from around a thousand 2D radiographs of the X-ray attenuation properties of the various materials forming the sample. As air in the fracture void and minerals in the rock matrix have different X-ray attenuation properties, they can be differentiated on the 3D images.

The X-ray source was diffracted through a double Si(111) crystal yielding a focused monochromatic and parallel beam with energy of 40 keV. The combination of an adapted optics with the CCD camera provides a spatial resolution of $6 \mu\text{m}$ for an optical resolution (pixel size) of $4.91 \mu\text{m}$. As the camera field is shorter than the height of the sample, only the upper part of the sample close to the inlet was scanned (Fig. 1b). Volume reconstruction was carried out from nine hundred 2048×2048 radiographs using direct Fourier inversion, through the use of a filtered back-projection algorithm (Herman, 1980). Radiographs were filtered prior to the reconstruction in order to eliminate the random noise due to high-energy diffracted photons, by substituting these noisy pixels with the median of their neighbours. The reconstruction provided six 3D image volumes of the X-ray absorption by the different materials in the sample, named V_0 to V_5 . Each volume is about $400 \times 2000 \times 1600$ voxels of volume $4.91 \times 4.91 \times 4.91 \mu\text{m}^3$ each.

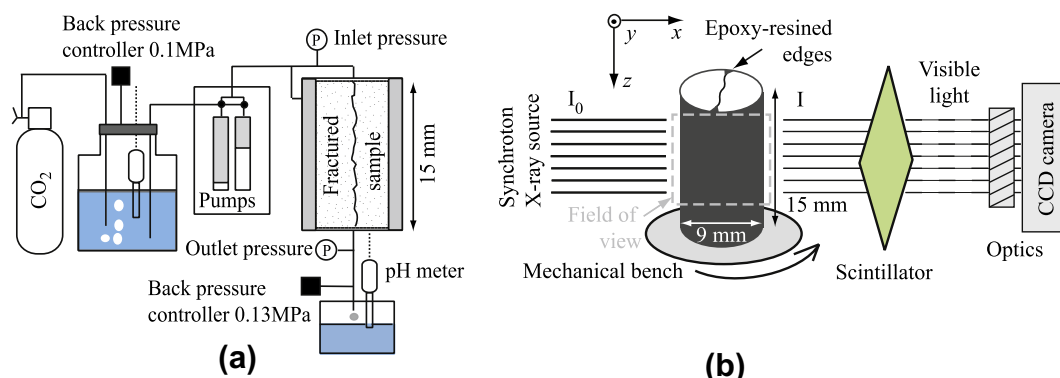


Fig. 1. (a) Schematic representation of the plug-flow apparatus and (b) field of view (10×10 mm) covered during X-ray micro-tomography imaging.

2.3.2. Image analysis

While the reconstructed image volumes were saved at 32-bit accuracy, they were first converted in 8-bit accuracy data sets to reduce the size of the original volumes without affecting the quality of the images. Then, the attenuation value takes a grey level value bounded by 0 (black) and 255 (white). By convention, dark voxels correspond to low density phases, whereas light voxels denote high density phases. The range of greyscale associated with a data set is variable because it depends on the X-ray beam intensity (which varies with time due to the fluctuation of the energy in the synchrotron accelerator ring), and the response of both the scintillator detector and the CCD camera.

As several data sets of the same sample were collected at increasing times, it was important to make sure that the method used to compare one data set to another is reliable even if X-ray beam intensity fluctuation exists. Assuming that the composition and the density of the fracture void and the carbonate matrix were unchanged (except for the fracture geometry modifications that occurred during the experiment), the difference in the X-ray attenuation was attributed to variation in the X-ray beam properties or to uncontrolled degradation in the conditions of acquisition. Accordingly, the histograms of grey level distribution were renormalised using a linear interpolation to adjust the minimum and maximum values at fixed values determined for the 3D volume at t_0 . Threshold values corresponding to 1% and 99% of voxels over the entire volume were also used to enhance the contrast of the images.

Another step to make the comparison of the volumes feasible is registration of the data sets in the same coordinate system. Although different methods have been developed to optimise the registration of two data sets, e.g. the minimisation function of the misfit (Ketcham and Iturrino, 2005), they are difficult to apply to large data sets and moreover to images that present many structural differences such as that resulting from dissolution. A linear transformation was applied, based on the identification of several control points on different data sets and determination of the (4×4) matrix that allows rotation and translation along the three

orthogonal planes. The different target volumes were aligned with the reference volume V_0 , using a tri-linear interpolation technique to calculate the grey value of the target voxels in the new coordinate system (Gonzales and Woods, 1992).

Then, in order to have a representation of the fracture void geometry and to quantify fracture parameters such as fracture wall topography, aperture distribution, and specific surface, the image volumes must be segmented in order to separate the different phases on the 3D images. The fracture description will strongly depend on the segmentation procedure. Although the grey level histograms show two peaks relative to voids and matrix, respectively, the transition between them is not sharp due to the inherent noise of the imagery technique and to finite volume effects. A simple grey-level thresholding method based on a cut-off value between the two peaks on the histogram would have led to significant errors and multiplication of the fluid–rock interfaces. Among the alternative methods developed to better separate the two phases, including noise reduction, edge enhancement and tracking, and region growing (Oh and Lindquist, 1999; Pitas, 2000; Sheppard et al., 2004), the region growing-based segmentation algorithm (Pitas, 2000) was preferred. A 3D median filter was applied to the different images volumes before the segmentation to reduce noise and allow a better separation of the two peaks of the histogram, while preserving the gradients (Nikolaidis and Pitas, 2001) and without affecting the boundaries between voids and matrix. The method presents the advantage of locating the edges separating the two phases where the gradients are stronger. At the end of the procedure, all the voxels were assigned a binary value, either 0 (void) or 1 (matrix). Fig. 2 presents the fracture geometry changes obtained using XMT after segmentation.

2.3.3. Extraction of the fracture wall topography and aperture

After segmentation, the different binary image volumes were percolated using a recursive grassfire algorithm (Gonzales and Woods, 1992) to progressively separate the connected fracture network from non-connected isolated pores. The fracture wall topog-

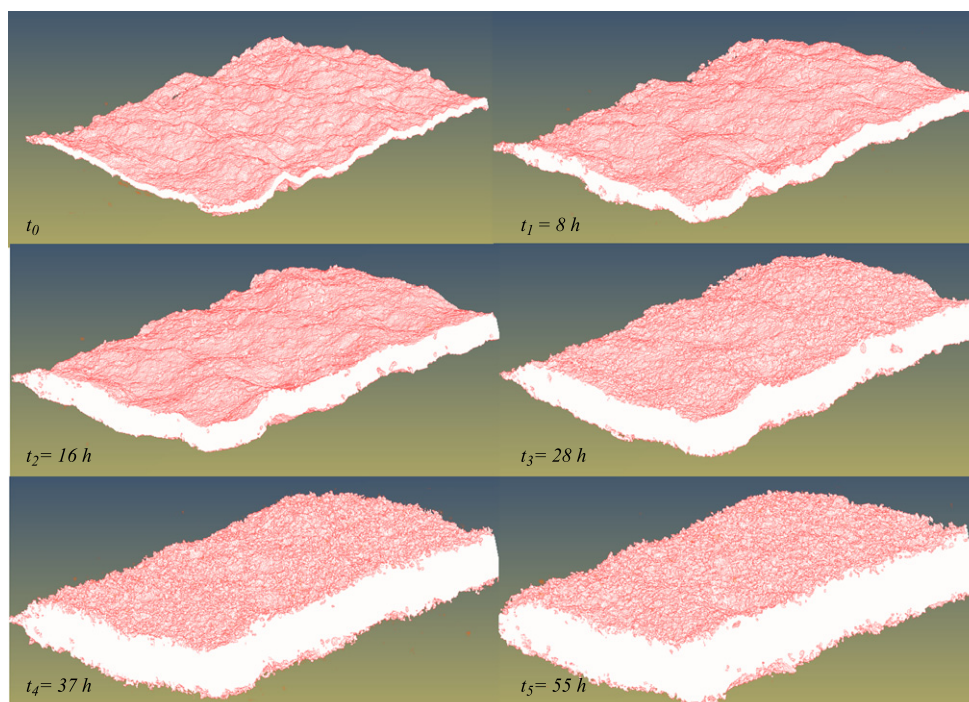


Fig. 2. 2×2 mm extract of the 3D fracture morphology at the different stages of the experiment (t_0 to t_5).

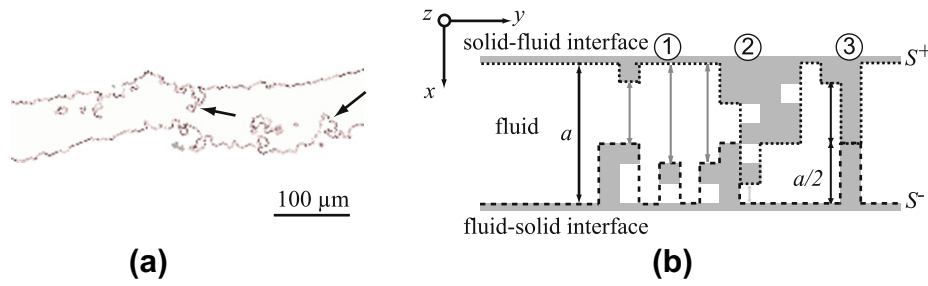


Fig. 3. (a) Observation of overlaps at the fracture surface and (b) schematic representation of the surface extraction procedure in the case where several fluid–rock interfaces exist. (1) Case where $x_1 > x_2$; (2) case where $x_1 = x_2 = x_3$; (3) case where $a = 0$.

raphy and aperture maps were then deduced from the connected fracture network.

As fracture walls locally display some overlaps (Fig. 3a), it makes the location of the fracture walls as the definition of fracture aperture a complex issue, as already mentioned by Gouze et al. (2003). However, roughness analysis methods require a single-valued function $h(y_i, z_i)$ of the elevation.

One approximation was chosen to obtain a single-value function when the fracture presents more than two fluid–rock interfaces, by reducing the sum of different fluid–rock interfaces to only two, as described below. The method leads to the identification of topography of the fracture walls comparable with what can be obtained using profilometry. The number and the length of the voids included between two solid pixels were determined when moving perpendicularly to the plane (\vec{y}, \vec{z}) for each (y, z) location. Only the longer void space was kept, the others were marked as solid pixels. In the case of several voids that had the same maximal length, only the last was arbitrarily kept. After this procedure, only two fluid–rock interfaces remained. Then the first fracture wall S1 was determined when a matrix voxel to void voxel interface is reached, for an elevation value of $h_{S1}(y_i, z_i)$. The second fracture wall was determined when a void voxel encounters a matrix voxel, for an elevation value of $h_{S2}(y_i, z_i)$. The topography of the two fracture walls was then obtained. In the case that no void was identified (null aperture), the position of the point of contact was set at half the elevation value of the neighbouring coordinates, i.e.: $h_{S1}(y_i, z_i) = h_{S2}(y_i, z_i) = [h_{S1}(y_{i-1}, z_i) + h_{S2}(y_{i-1}, z_i)]/2$. A schematic representation of the procedure is presented in Fig. 3b.

Before statistics calculation, the mean plane of the fracture was calculated from a least square fitting method and subtracted from the raw data. Under this assumption, the mean value of the upper surface elevation S1 is opposite to the mean value of the under surface elevation S2, i.e. $\langle h_{S1} \rangle = -\langle h_{S2} \rangle$. The opening of fracture or local aperture, a , is defined as the separation between two fracture walls at any given value of (y, z) perpendicularly to the plane (\vec{y}, \vec{z}) .

3. Data analysis

3.1. Aperture and fracture walls characterisation from XMT

The morphology of the fracture was evaluated in course of dissolution using several criteria, including statistical parameters. The aperture distribution $a(y, z)$ of the fracture of side length L and width l is described by the discrete aperture distribution sampled on a regular $4.91 \times 4.91 \mu\text{m}$ grid. Average values of aperture for each profile along the y - and z -directions are defined as $\langle a \rangle_y$ and $\langle a \rangle_z$, respectively. The mechanical aperture a_m is the mean of the local apertures:

$$a_m = \langle a \rangle_{yz} = \frac{1}{Ll} \int_{y=0}^l \int_{z=0}^L a(y, z) dy dz \quad (1)$$

The standard deviation of aperture σ_a is an appropriate parameter to qualify roughness changes at the fracture scale. The macroscopic roughness factor a_m/σ_a quantifies the degree of aperture variability. This parameter is commonly used to characterise the relative roughness of a fracture and to quantify the departure of normalised permeability from the cubic law (Brown, 1987; Méheust and Schmittbuhl, 2001; Patir and Cheng, 1978; Zimmerman et al., 1991). In the parallel plate model, the ratio a_m/σ_a tends toward infinite value. When roughness increases, i.e. a_m/σ_a decreases, deviation from the cubic law is expected.

Another parameter used is the roughness coefficient, \mathfrak{R} , calculated using the square root quadratic mean of the asperity heights of the aperture (\mathfrak{R}_a) or the fracture walls (\mathfrak{R}_s). As shown by Myers (1962), the variation of the roughness coefficient \mathfrak{R} with time seems to be a convenient parameter to quantify the roughness changes at micro-scale. For a profile of elevation h , (h being either the aperture or the fracture wall elevation) along the flow axis, it is given by:

$$\mathfrak{R} = \sqrt{\frac{1}{Ll} \sum_{y=1}^{y=l} \sum_{z=1}^{z=L} (h_{z+1} - h_z)^2} \quad (2)$$

The tortuosity, τ , quantifies the length of the different profiles compared to their mean reference line. For a profile of elevation h along the flow axis, it is given by:

$$\tau = \frac{1}{l} \sum_{y=1}^{y=l} \frac{L'}{L} = \frac{1}{l} \sum_{y=1}^{y=l} \frac{\sum_{z=1}^{z=L} \sqrt{(h_{z+1} - h_z)^2 + \Delta z^2}}{L} \quad (3)$$

Semi-variograms are also used to study the spatial correlation structure of the fracture aperture (Hakami and Larsson, 1996). Semi-variance along the flow axis is calculated according to:

$$\gamma(\delta) = \frac{1}{2n} \sum_{i=0}^{i=n} [a(z_i + \delta) - a(z_i)]^2 \quad (4)$$

were δ is the lag distance, n the number of observation pairs, $a(z_i)$ the aperture taken at the location z_i , and $a(z_i + \delta)$ the aperture taken δ intervals away. When δ is small, the apertures $a(z_i)$ and $a(z_i + \delta)$ tend to be very similar, consequently leading to small semi-variance values. The correlation between $a(z_i)$ and $a(z_i + \delta)$ decreases as far as the lag distance increases. At some lag distance, the apertures being compared are too far apart to be correlated. In the case of a stationary process, the semi-variance reaches a plateau value (the sill, s) which becomes equal in magnitude to half of the variance of the aperture. The lag distance at which the semi-variance approaches the sill is referred as the spatial correlation length (the range, r) of the fracture aperture. It defines the interval in which the apertures are closely correlated to each other.

Finally, the roughness exponent H (or Hurst exponent) was calculated from the power spectrum density of the different fracture walls, as the self-affine character of many rock surfaces has been demonstrated by experimental observation (Brown and Scholz,

1985; Schmittbuhl et al., 1995). The power spectrum shows a decreasing power law of the form: $G(k) = ck^{-1-2H}$ if the profiles have fractal properties; here H represents the Hurst exponent, c is a constant, k is the frequency.

3.2. Fluid flow simulations

The numerical CFD package Fluent[®], based on the finite-volume method, was used to solve the flow equations in a 8.84×7.78 mm region of the fracture at t_0 to t_5 . The momentum equation was solved using a second-order upwind scheme. A computational grid of 415,800 nodes was generated from the two fracture walls extracted from the XMT image volumes. Pixel size renormalisation (initially $4.91 \mu\text{m}$ in all directions) was applied to allow tractable computation of the 3D flow field. A uniform square mesh fracture geometry of 157×132 elements of size $58.92 \mu\text{m}$ in the y - z plane was created. The fracture aperture (x -direction) was meshed by 20 elements of variable size to reproduce a parabolic function from the fracture wall to the middle in order to refine the grid in the areas of higher flow gradient and correctly simulate the quasi-Poiseuille flow distribution across the fracture. The boundary conditions were taken to be constant flow rate ($Q = 100 \text{ cm}^3 \text{ h}^{-1}$) at the sample inlet, uniform pressure ($P = 0.1 \text{ MPa}$) at the outlet, and no flux at the fracture walls. The 3D velocity and pressure fields were obtained by solving the Navier–Stokes equation system in steady-flow. From the data, x -averaged values of the fluid pressure and velocity between sample inlet and outlet were calculated and used to evaluate the simulated hydraulic aperture a_{h-NS} using the cubic law (Eq. (A.2)).

3.3. Quantitative determination of the extent of the reaction

The volume of calcite removed by the sample during dissolution can be evaluated from calcium flux or concentration at the outlet:

$$\frac{\delta V_{\text{calcite}}}{\delta t} = -F_{\text{Ca}} \times v_{\text{calcite}} = -Q \times \frac{\delta(\Delta \text{Ca})}{\delta t} \times v_{\text{calcite}} \quad (5)$$

with $\delta V_{\text{calcite}}$ the variation in volume of calcite (m^3), F_{Ca} the flux of calcium at the sample outlet (mol s^{-1}), v_{calcite} the molar volume of calcite ($\text{m}^3 \text{ mol}^{-1}$) and ΔCa the variation in calcium concentration between the inlet and the outlet of the sample (mol m^{-3}).

As the sample has a 90% calcite composition, the theoretical rate of aperture increase (m s^{-1}) can also be calculated from the amount of calcium removed by the fluid in the fracture, assuming that the dissolution of the fracture walls was uniform:

$$\frac{\delta a_c}{\delta t} = \frac{1}{0.9 \times A_s} \times \frac{\delta V_{\text{calcite}}}{\delta t} = -\frac{Q}{0.9 \times A_s} \times v_{\text{calcite}} \times \Delta \text{Ca} \quad (6)$$

where a_c is defined as the chemical aperture and $A_s = l \times L$ is the planar surface area of the fracture wall (m^2). From the knowledge of the initial value of aperture which is set to the value of a_m at t_0 , the chemical aperture a_c at time t is calculated by integrating Eq. (6). The measurement of a_c gives additional information about the dissolution process at the sample scale based on mass balance, and is helpful to test the accuracy of the XMT method, as a_m and a_c should be similar.

4. Results

Coupling the flow-through experiment with XMT observation provides three independent evaluations of the parameters characterising the dissolution process within the fracture, from micro-scale to sample-scale. Chemical composition of the outlet solution characterises the overall dissolution kinetics. Differential pressure measurement between the sample inlet and outlet allows quantification of hydraulic aperture. In addition, XMT provides

imaging of the fracture geometry changes associated to reactive transport.

4.1. Solution chemistry

The calcium concentration of the outlet solution (or the Ca flux) is directly related to the rate of dissolution over the length of the sample. The outlet solution remains highly undersaturated with respect to calcite, with a saturation index Ω decreasing from -4.02 to -5.12 on a log scale (data were obtained with Chess using the CTDTP thermodynamic database (Common Thermodynamic Database Project, (van der Lee and Lomenech, 2004, <http://www.ctdtp.org>)). The temporal evolution of the different elements concentration fluctuates but progressively decreases with time (Fig. 4), except Ba, B and Rb (Fig. 4b). A correlation is found between B and Rb concentrations and another between Ca, Mg, Ba, and Sr concentrations. Concentrations of B and Rb, which are generally associated with the clay fraction, indicate that the contribution of clays to the dissolution is quite steady with time. However, despite Ca, Mg, Ba, and Sr are all being assumed to be products of the dissolution of carbonates, the correlation is far from the perfect correlation expected during congruent dissolution of calcite at low pH, indicating that (i) the different calcite crystals present different chemical compositions, and (ii) Ca, Mg, Ba, and Sr concentrations result from a convoluted signature of the contribution of the different carbonate grains of variable composition to the dissolution.

4.2. Dissolution patterns

At the sample scale, XMT observations reveal that the dissolution acts on the whole as chemical erosion. The fracture aperture patterns are mainly preserved (Fig. 5), although some heterogeneities of dissolution linked to the coupled chemical reactions and transport phenomena are observed. The dissolution is enhanced near the sample inlet (Fig. 6a) as a consequence of the decrease of the pH-dependent kinetic rate of calcite dissolution (Plummer et al., 1978) as far as the reaction progresses through the sample. Also, the dissolution rate is progressively reduced close to the edges of the sample (Fig. 6b), which results from slower flow velocities in these areas (boundary effects).

At the micro-scale, a close examination of the XMT data sets as a cross-section of the sample after experiment show that the fracture walls dissolved in a non-uniform manner during the experiment. The difference of dissolution kinetic rates between minerals of different composition triggers the increase of the heterogeneity of the fracture walls dissolution and consequently increases the roughness. Micro-crystalline calcite dissolves more quickly than biogenic sparite crystals, and far more quickly than quartz and clays, which can be considered as non-reactive at the time scale of our experiment. However, contrary to what (Noiriel et al., 2007b) observed during dissolution of an argillaceous limestone with similar experimental conditions (i.e. inlet solution chemistry and flow rate) but higher clay content (roughly 25% silicate minerals), only slight evidence of silicates was noticed in the fracture void, indicating that they are progressively removed from the surface and transported as a solid phase. As a result, clays do not interfere globally with the calcite dissolution process, but certainly contributes to head loss stagnation in the fracture and might also affect transport of elements close to the fracture walls (see discussion below).

4.3. Statistical analysis of the fracture geometry

4.3.1. Aperture

Results of fracture aperture measurements using X-ray microtomography are presented at the different experiment stages as

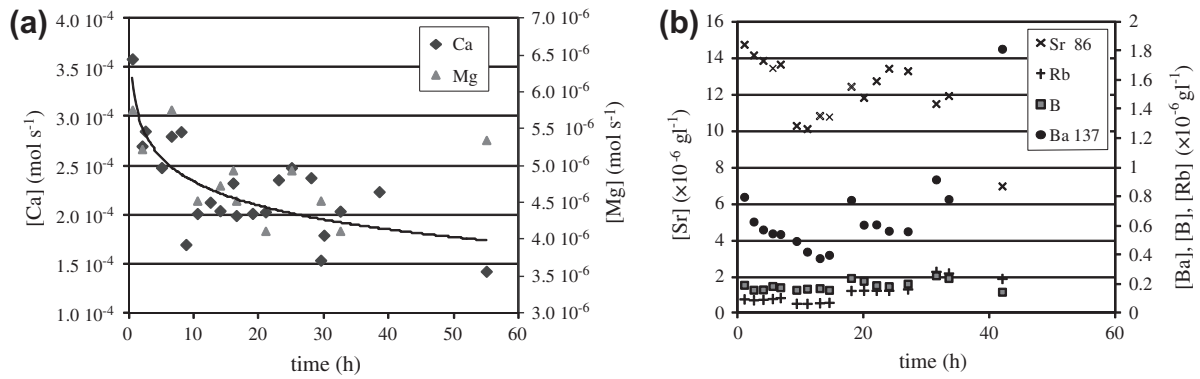


Fig. 4. (a) Calcium and magnesium flux with time (mol s^{-1}). (b) Composition of the outlet solution in minor elements.

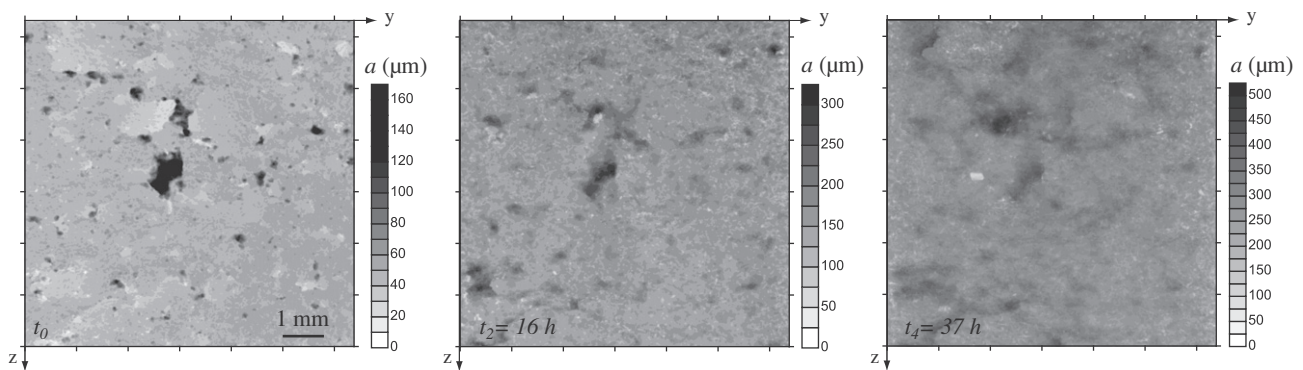


Fig. 5. Maps of fracture aperture at t_0 , t_2 and t_4 .

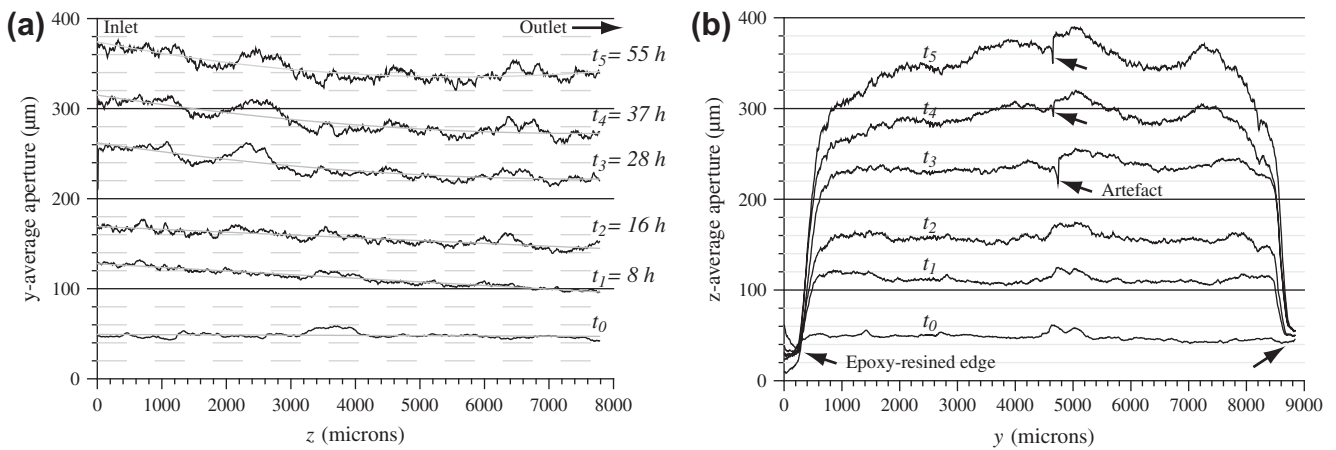


Fig. 6. Plots of the average aperture (a) along the flow ($\langle a \rangle_z$) and (b) perpendicular to flow ($\langle a \rangle_y$) at the different stages of dissolution. Note that the disconnection visible near the middle of the curves is due to an artefact of imagery, which is present near the rotation axis of the sample, and affects very locally the calculation of the average aperture.

summary statistics in Table 1, as digital images in Fig. 2 and as frequency histograms in Fig. 7. The mechanical aperture (a_m) increases from $48.3 \mu\text{m}$ (t_0) to $346.4 \mu\text{m}$ (t_5). The standard deviation σ_a increases with increasing dissolution. As a consequence, the frequency histogram of aperture becomes more and more flat and large (Fig. 7). At t_0 , the aperture distribution (a) is bell-shaped, with a low percentage of zero-aperture (0.005%). Although several authors have observed log-normal distributions of the aperture (Bertels and DiCarlo, 2001; Bloomfield, 1996; Keller, 1998; Walters et al., 1998), the histogram suggests that a normal distribution could be the most appropriate model for

characterising the aperture distribution in the sample, even if the histogram has a stronger pick compared to a normal distribution, with a positive kurtosis equal to 14.6. The skewness is positive, indicating that the data are skewed toward high aperture values. It arises from the fact that aperture measurement is bounded at the low values by zero. During the dissolution process, the distributions remain bell-shaped, but kurtosis and skewness both progressively decreased and the distribution leads progressively to a normal distribution (Fig. 7).

Although σ_a increases during the experiment, the effect of dissolution causes the macroscopic roughness factor (a_m/σ_a) to

Table 1

Statistics of aperture and surface distribution.

Time (h)	$t_0 = 0$	$t_1 = 8$ h	$t_2 = 16$ h	$t_3 = 28$ h	$t_4 = 37$ h	$t_5 = 55$ h
$a_m = \langle a \rangle_{yz}$ (μm)	48.3	112.2	157.3	235	287.4	346.4
σ_a	14.1	21.4	29.7	33.6	43.7	53.0
a_m/σ_a	3.45	5.26	5.26	7.14	6.67	6.67
Kurtosis	14.62	2.68	1.96	3.02	1.53	0.68
Skweness	3.77	2.00	1.77	2.05	1.69	1.44
\mathfrak{R}_a	0.92	1.86	2.82	2.58	3.66	4.55
τ_a	1.26	1.65	2.04	2.03	2.57	3.01
σ_{s1}	102.2	102.6	103.9	104.1	108.0	110.4
σ_{s2}	102.6	104.3	104.7	103.7	103.5	102.0
σ_s	102.4	103.5	104.3	103.9	105.8	106.2
\mathfrak{R}_s	1.23	1.42	2.08	1.86	2.68	3.29
a_m/σ_s	0.47	1.08	1.51	2.26	2.72	3.26

increase (Table 1), suggesting that relative roughness decreases. As a result, deviations from the cubic law would not be expected. The tortuosity and the roughness coefficient also increase, from 1.26 to 3.01 and from 0.92 to 4.55, respectively.

The spatial correlation of the aperture was also analysed from the experimental semi-variograms (Fig. 8a). Results taken in the direction parallel or perpendicular to the flow direction are very

similar. Initially, the semi-variogram can be almost perfectly fitted by an exponential model: $\gamma(\delta) = \text{sill} \times [1 - \exp(3\delta/\text{range})]$, with a sill of 200 μm and a range of 630 μm ; the correlation length, λ_a , is equal to 1/3 of the range, i.e. 210 μm . From t_0 to t_3 , the sill increases from 390 μm (t_1) to 930 μm (t_3). All the correlation lengths are small relative to the overall dimension of the sample. However, the exponential model does not fit so well the data, which show higher values of the semi-variance at the small scale ($0 \leq \gamma(\delta) \leq 200$) compared to an exponential model with the same range as t_0 . In other words, the correlation length of the aperture remains almost equal while changes occur at the small-scale and variance increases in response to the heterogeneous dissolution (Fig. 8a). From t_3 the semi-variograms do not develop sills, indicating that the data are non-stationary and that the variance is not finite and constant.

4.3.2. Fracture walls

Statistics of surface topography measurements are also reported in Table 1. The standard deviation σ_s remains quasi constant with time. Only a slight increase is observed, from 102.4 (t_0) to 106.2 μm (t_5). One can also see that the value of standard-deviation is slightly different for each of the surfaces S1 and S2.

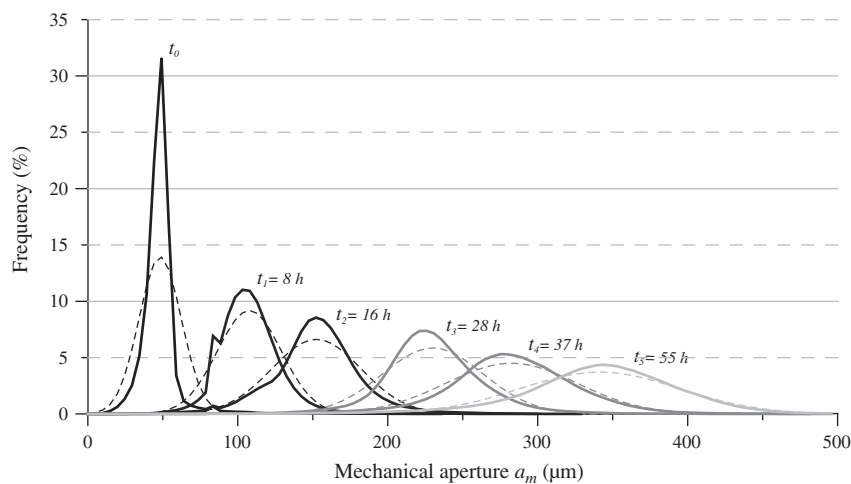


Fig. 7. Distribution of the mechanical aperture (bold) and comparison with a normal distribution (dotted line) at the different stages of experiment.

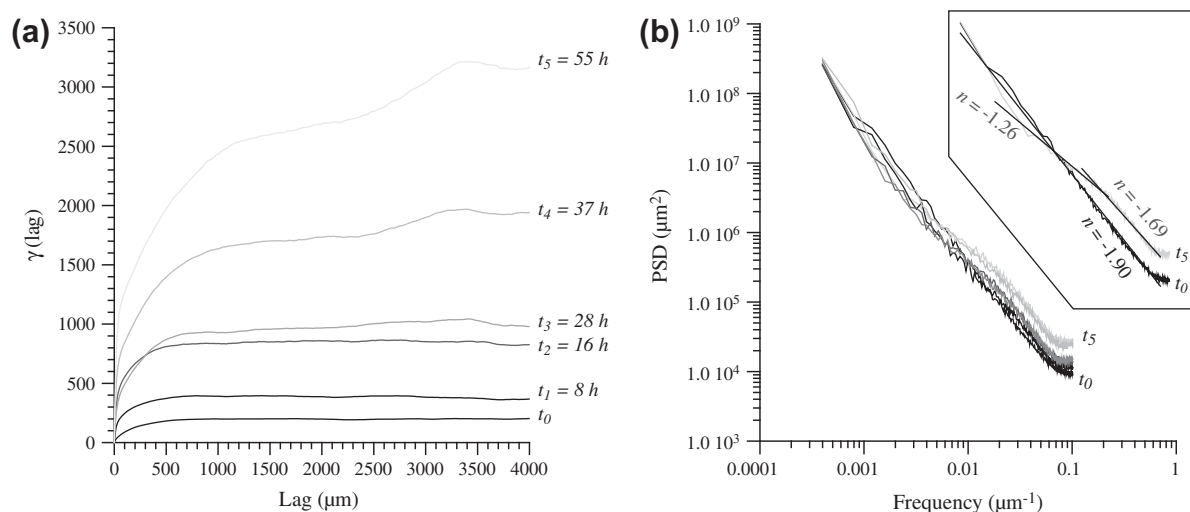


Fig. 8. (a) Semi-variogram of aperture and (b) power spectrum density (PSD) of the fracture wall S1 at the different stages of experiment. In box: detail of the PSD and slopes of the power fits at t_0 (one slope of equation $n = -1.90$) and t_5 (two slopes of equation $n = -1.26$ and $n = -1.69$).

Conversely, the microscopic roughness (i.e. the roughness factor \mathfrak{R}_s), which can be characterised by the local variation of topography, increases largely during the experiment, from 1.23 (t_0) to $3.29 \mu\text{m}$ (t_5). According to the procedure used to determine the surface topography of the fracture (see Section 2.3.2), the increase of the value of \mathfrak{R}_s is linked to roughness increase or development of overlaps at the surface. In both cases, an increase of the complexity of the fracture surface topology is measured. Conversely, the ratio

of aperture to standard-deviation of the surfaces, a_m/σ_s , increases with time, from 0.47 to 3.26, indicating that the surface roughness should impact the flow less and less.

Before the experiment, the two surfaces display a fractal behaviour with a Hurst exponent equal to 0.5 (Fig. 8b). The dissolution process induces a break in the slope of the power spectra at a frequency of around $0.08 \mu\text{m}^{-1}$, indicating that high wavelength fluctuations are unchanged while changes occur at the small scale.

Table 2
Comparison between the measurement of three distinct types of aperture (a_m , a_c , and a_h), the aperture obtained from numerical simulations (a'_h), and the aperture derived by Patir and Cheng (1978) from Reynold's equation (a_{h-REY}). The value of the x -average fluid velocity ($\langle u_{z,x} \rangle$) and corresponding standard deviation ($\sigma_{(u_{z,x})}$) obtained from numerical simulations is also given.

Time (h)	$t_0 = 0$	$t_1 = 8 \text{ h}$	$t_2 = 16 \text{ h}$	$t_3 = 28 \text{ h}$	$t_4 = 37 \text{ h}$	$t_5 = 55 \text{ h}$
a_m (μm)	48.3	112.2	157.3	235.0	287.4	346.4
a_c (μm)	48.3 ^a	102.4	163.1	240.8	300.0	391.1
a_h (μm)	22	20	50	90	–	–
a_{h-NS} (μm)	42.3	90.8	135.4	200	240.7	289.0
a_{h-REY} (μm)	44.3	105.3	147.2	221.2	269.5	324.2
$\langle u_{z,x} \rangle$ (m s^{-1})	6.77×10^{-2}	2.92×10^{-2}	2.05×10^{-2}	1.37×10^{-2}	1.11×10^{-2}	9.06×10^{-3}
$\sigma_{(u_{z,x})}$	1.69×10^{-2}	8.67×10^{-3}	5.97×10^{-3}	4.05×10^{-3}	3.52×10^{-3}	3.07×10^{-3}

^a As a_c is unknown at t_0 , the value was set to the initial value of a_m .

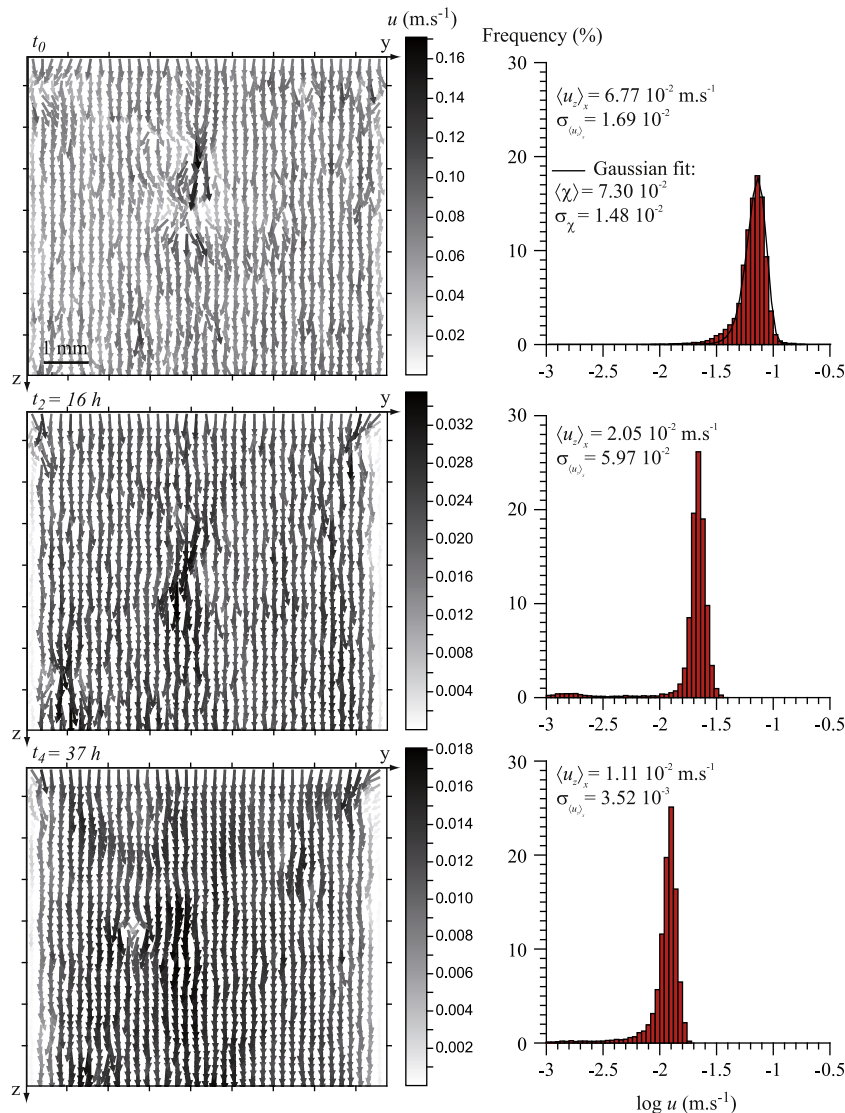


Fig. 9. Maps of flow velocity averaged at t_0 , t_2 and t_4 and corresponding histograms (in a log scale).

This observation confirms the results given by statistical analysis, meaning that surface roughness increases at the small scale but not at the large scale.

4.4. Hydraulic aperture

The initial equivalent hydraulic aperture a_h is equal to 22 μm (Table 2). From t_4 , ΔP is too low to calculate the hydraulic aperture. During the experiment, the hydraulic aperture increases step by step, especially between two different stages of experiment. That can be linked to the behaviour of silicates at the fluid–rock interface while the carbonates dissolve. Clays certainly remain stuck at the fluid–rock interface until the surrounding matrix is completely dissolved or the flow conditions are high enough to pull them out of the surface. This assumption is supported by the fact that removal of ochre clay particles was observed during resaturation of the sample after every XMT acquisition, for which the sample was removed from the flow-through cell and slightly desaturated.

4.5. Evolution of the flow field and flow patterns

Maps of flow velocities averaged in the x -direction are presented in Fig. 9 to provide a 2D flow representation. The hydraulic aperture a_{h-NS} and the x -averaged velocity $\langle u_z \rangle_x$, both obtained from the numerical simulations, are presented in Table 2. As far as the mechanical aperture increases, both the velocity and the velocity variability, $\langle u_z \rangle_x / \sigma_{\langle u_z \rangle_x}$, globally decrease. The flow field is initially (t_0) heterogeneous and the highest velocities are reached in a small area of the fracture where the aperture was initially higher. With the exception of the lowest velocities, the x -averaged velocity distribution is initially (t_0) approximately a normal distribution of average $\langle \chi \rangle = 0.073$ and standard deviation $\sigma_\chi = 0.0146$. As a result of dissolution, velocities decrease, and the distributions become more heterogeneous with a main mode more peaked and a tail of low velocities (as fluid velocity remains very low near the fracture edges).

Despite the flow field being heterogeneous, no evidence of flow channelling was noticed, neither initially nor after dissolution. Normally, reactive transport would have led to flow localisation and enhanced dissolution in the area of initial higher fluid velocity, as a result of positive feedback between flow and reactive transport (Ortoleva et al., 1987; Steefel and Lasaga, 1990). Indeed, the dissolution of calcite at low pH values is transport-limited, so that the dissolution should be enhanced in the areas of higher fluid velocity. However, in the present case, the area of initial higher flow velocity progressively disappears amid several small areas where flow is enhanced.

The water flow patterns and their changes were also characterised by the velocity profiles. The shapes of the velocity profiles between the two fracture walls were compared to the parabolic profiles which are defined for the parallel plate model by: $u_z(x) = u_0(1 - (2x/a)^2)$, where u_0 is the maximum fluid velocity. For the parallel plate model, the profiles are centred, the average velocity in the flow direction is equal to: $\langle u_z \rangle_x = u_0/3$, and the parabolas have a symmetric shape, so that \vec{u}_0 is collinear to the mean aperture axis plane \vec{z}_0 ($\vec{u}_0 = k\vec{z}_0$). However in real fracture, particularly if the fracture displays sharp geometries, the parabolic velocity profiles are not necessarily symmetric with respect to the fracture walls (Dijk et al., 1999; Tenchine and Gouze, 2005). In that case, the profiles can be either asymmetric (then, $\langle u_z \rangle_x = u_0/3$, but u_0 is not collinear to the mean aperture axis plane, i.e. $\vec{u}_0 \neq k\vec{z}_0$) or distorted non-parabolic (then $\vec{u}_0 \neq k\vec{z}_0$ and $\langle u_z \rangle_x \neq u_0/3$). The proportion of centred parabolic profiles (CPP), asymmetric parabolic profiles (APP) and non-parabolic profiles (NPP) was calculated at each stage of the experiment (Fig. 10, see Tenchine and Gouze,

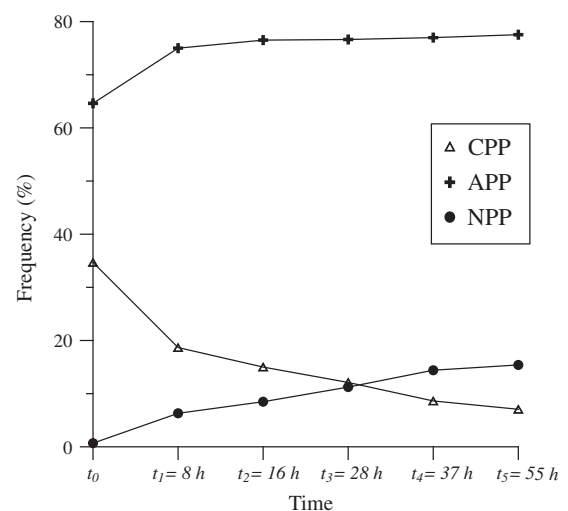


Fig. 10. Velocity profiles (i.e. centred parabolic profiles (CPP), asymmetric parabolic profiles (APP) and non-parabolic profiles (NPP)) in the fracture at the different stages of experiment.

2005 for more details). Initially (t_0), CPP represents 35% and APP 65%. The large value of APP results both in the complex geometry of the fracture and aperture roughness. At t_1 , CPP represents only 19%, and APP and NPP increase to 75% and 6%, respectively. As the fracture dissolves, CPP continues to decrease (up to 7% at the end of experiment), APP remains almost constant, and NPP increases consequently (up to 15% at t_5). The increase of the NPP while CPP decreases can be linked to the roughness increase and progressive decorrelation of the fracture walls.

5. Discussion

By combining the reactive flow-through dissolution experiment with fracture geometry characterisation, a direct comparison is possible between chemical, geometrical and hydraulic (from both experiments and numerical simulations) properties. The advantage of XMT is that the technique has proved its accuracy for directly comparing the changes of rock geometry by image subtraction or for measuring porosity differences of less than 1% (e.g. Noiriel et al., 2004). From the 3D images it is possible to characterise the flow in both the fresh and altered fracture. Discussed below are the implications of dissolution in mineralogically heterogeneous rocks on the fracture dissolution patterns, flow, and reactive transport.

5.1. Flow

The three distinct measurements of aperture, i.e. mechanical aperture a_m calculated from X-ray micro-tomography imaging, chemical aperture a_c obtained from calcium concentration measurement and hydraulic aperture a_h deduced from the hydraulic test, are compared to the computed hydraulic aperture a_{h-NS} calculated using flow simulation and aperture a_{h-REY} derived from Reynolds' assumption in the fracture void geometry (Eq. (7), see below). Results are presented in Table 2 and Fig. 11.

From the experiment, it is shown that a_m and a_c are quite in a good agreement (except at t_5), but differ from a_h (Table 2). The discrepancy between a_h and a_m is explained by the presence of clays which can hinder the flow in the fracture void (see Section 4.4), and has already been observed during other dissolution experiments on fractured carbonate rock samples containing clays (Ellis et al., 2011; Noiriel et al., 2007b).

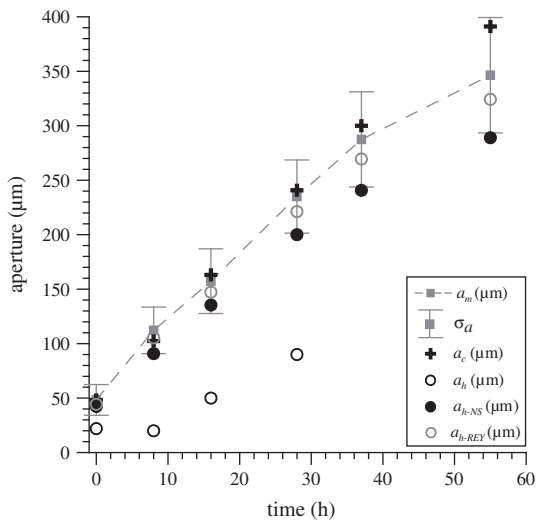


Fig. 11. Apertures as a function of time.

The parallel plate assumption implies that both fracture roughness and tortuosity play no role in affecting fluid flow. However, the geometry of a natural fracture diverges more or less from the parallel plate model, and deviations to the cubic law can be assessed through the comparison between the hydraulic aperture calculated by numerical simulation (a_{h-NS}), and the mechanical aperture (a_m). Using finite differences to resolve the local cubic law equation, Patir and Cheng (1978) performed flow calculation between surfaces whose profiles obeyed a Gaussian distribution with a linearly-decreasing autocorrelation function. The authors found that the hydraulic aperture calculated from the Reynolds' equation (a_{h-REY}) could be fitted by an exponential relation:

$$a_{h-REY}^3 = a_m^3 (1 - 0.9 \exp(-0.56 a_m / \sigma_a)) \quad (7)$$

In their model, deviation from the cubic law is expected when a_m / σ_a is below a value of 10. Results obtained by Brown (1987) using similar calculations on several generated fractal fractures with different fractal dimensions (from 2.0 to 2.5), and Zimmerman and Bodvarsson (1996) using high-order approximations for lognormal distribution of permeability, fall close to Eq. (7). Their results suggest that the formula is applicable to fractures with different geometrical characteristics.

In Table 2, the hydraulic aperture calculated by Navier–Stokes simulation (a_{h-NS}) differs by between 12% (at t_0) and 19% (at t_1) from the mechanical aperture. The hydraulic aperture calculated using Eq. (7), a_{h-REY} , differs also from the mechanical aperture, from 6% (t_1 to t_5) to 8% (t_0), while the ratio a_m / σ_a slightly increases from t_0 to t_5 ($3.45 \leq a_m / \sigma_a \leq 6.67$).

Initially, the deviation from the cubic law is explained by the sample-scale roughness and tortuosity of the fresh fracture. As the ratios a_m / σ_a and a_m / σ_s increase during dissolution, it is expected that the flow can be progressively idealised with the parallel plate model. However, even if the ratio a_m / σ_a certainly increases, it actually results in the concomitant increase of both a_m and σ_a . In that case, the situation is different from the study of Patir and Cheng (1978), where changes in roughness were involved only by changes in σ_a while a_m was kept constant. In our case, flow field in the fracture evolves away from the theoretical flow field assumed in cubic law, as shown by the shape of the velocity profiles (Fig. 10), which become more and more different from the centred parabolic profiles characterising flow in two parallel plates. So, it appears that the use of a_m / σ_a is not appropriate to characterise flow in altered fractures, when decorrelation of the fracture aperture and micro-roughness increase are observed.

However, it seems that deviation from the cubic law results principally from the decorrelation of the fracture aperture compared to the micro-roughness increase. Actually, there is no correlation between deviation of the cubic law and the roughness factor \mathcal{R}_s , which could indicate in first approximation that roughness increase at the small scale has no impact on permeability or deviation from the cubic law. However, it is worth noting that sub-sampling the fracture wall topography leads to surface smoothing. As a result, the small fracture wall features like micro-scale roughness were not captured during the meshing procedure, whereas step-by-step changes of a_h during the experiment rather suggest that micro-scale roughness affects the permeability of the sample, at least until the silicates are pulled out from the surface and transported as a solid phase.

5.2. Implication of mineralogy on flow, dissolution patterns, and reactive transport

The fracture roughness increase results from the difference in dissolution rates of the different calcites (i.e. micro-crystalline calcite and recrystallized biogenic fragments) and silicates forming the rock. It is clear that the silicates play a role on flow, explaining why the hydraulic aperture a_h did not increase regularly. In addition, dissolution involves some changes in macroscopic fluid flow, and particularly distortion of the velocity profiles, as shown by the proportion of initially centred parabolic flow velocity profiles which are turned into asymmetric or non-parabolic profiles. These changes can be linked to the alteration of the fractal surface model (Fig. 8b) and the decorrelation of both the aperture and fracture walls.

However, under the high flow rate of the experiment ($100 \text{ cm}^3 \text{ h}^{-1}$), it seems that the silicates do not influence the macroscopic dissolution patterns, conversely to what was observed by Noiriel et al. (2007a) during a similar experiment using the same rock as starting material, but at lower flow rate ($10 \text{ cm}^3 \text{ h}^{-1}$). In that case, a micro-porous phase formed by the silicates was observed in some areas of the fracture void, while it was completely removed elsewhere, leading to the formation of preferential flow channels. In that case, the formation of preferential flow channels did not result from a positive feedback between chemistry and transport, but from a relationship between fluid flow and cohesion forces of the clays.

Noiriel et al. (2007a, 2007b) already investigated dissolution effects in limestone rocks with different mineralogical compositions. For a sample composed of around 75% carbonates (essentially calcite) and 25% silicates (mainly clays, with a minor amount of quartz), dissolution of carbonates led to a clay coating growth

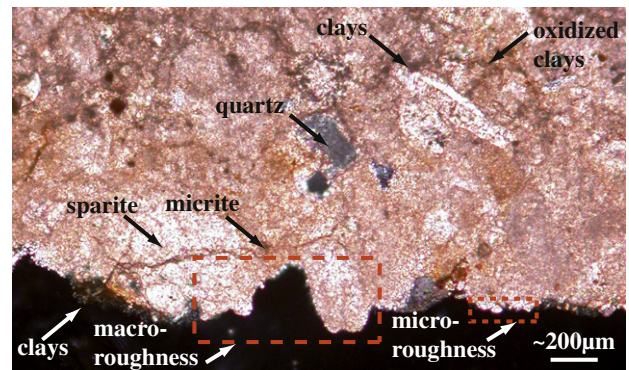


Fig. 12. Microscopy observation of the fracture wall cross-section of the sample after experiment, showing heterogeneous dissolution rates between micrite, sparite and clays.

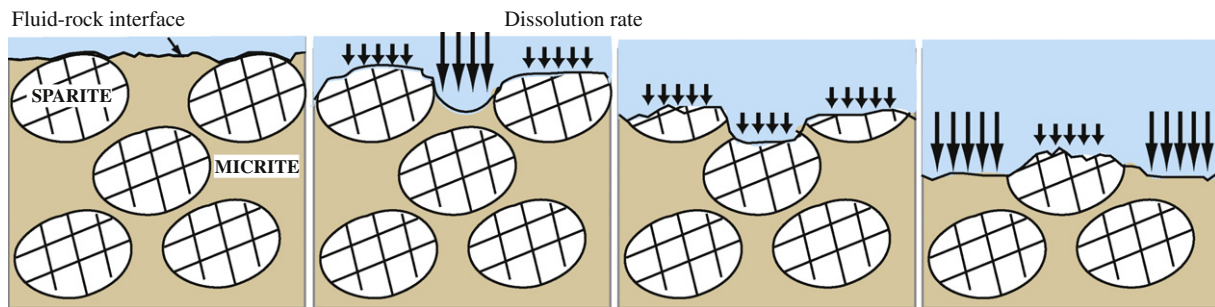


Fig. 13. Simplified sketch showing how calcite grains with different dissolution rates can affect the fracture wall roughness changes.

which acted as a diffusive barrier to the transport of elements through the micro-porous clay coating. As a result, the flux of Ca at the sample outlet progressively decreased with increasing dissolution. In our experiment, the chemical flux of Ca both slightly decreases and is fluctuating with time. As the flow regime is very dispersive throughout the experiment (Pe values ranging from 7.9×10^2 at t_0 to 7.1×10^2 at t_5), changes in Ca flux are more likely linked to effects of mineral heterogeneous dissolution rather than to macroscopic flow changes inherent to aperture increase (i.e. flow velocity and dispersivity). Firstly, the presence of different calcite crystals with different sizes and, therefore different reactive surface areas can lead to changes in the rate of calcite dissolution at the surface, affecting roughness of the fracture walls. This assumption is confirmed by microscope observations, where micrite is shown to be dissolved faster than sparite (Fig. 12). For a stochastic distribution of the calcite grains, the effects should offset on the long term (Fig. 13), but a sedimentary rock texture is rarely homogeneous (Noiriel et al., 2009). Secondly, the presence of clays at the surface (until they are removed from the fracture walls) can locally affect the flow field close to the fracture walls. Despite fluid flow seeming not to be sensitive to the micro-scale roughness (Fredrich et al., 2006), the diffusive flux toward and away from the surface can be affected because of the presence of dead zones or eddies. Indeed, distribution of species within the fracture results in a dynamic interaction between the bulk flow transport via advection and diffusion far away from the zones of fluid stagnation and transport out and into these dead zones mainly via diffusion. The access of reactants to the calcite surface and the departure of the reaction products from the surface are impeded by the fracture wall micro-roughness and overlaps which have developed at the surface. In particular, the global dissolution rate can greatly change when a partial of or complete control of the rate by molecular diffusion exists (Noiriel et al., 2012; Sugano, 2008). The solute distribution in dead zones was also shown to be particularly heterogeneous at large Pe (Cardenas et al., 2009). In addition, distortion of the velocity profiles across the fracture aperture could also have a significant impact on transport behaviour, as shown by Koyama et al. (2008). Then, despite they are suspected of affecting flow and reactive transport, it is difficult to evaluate the influence of silicates, in regards to the rock composition and Peclet value in the fracture. Nevertheless, their presence might explain why there was no development of preferential flow pathways in the areas of higher fluid velocity (see Section 4.5), and further investigations of transport at the micro-scale is needed to better understand the complex transport of solute species at the fracture surface.

6. Conclusions

The objective of the study was to better understand the relationship between fracture void geometry and flow changes during dissolution process, so that a direct comparison could be made

between geometrical and hydraulic property changes. X-ray micro-tomography has been shown to be an effective tool to non-destructively extract and quantify the geometry of fracture after an appropriate image processing procedure. Differences in the kinetic rates of the mineral forming the rock led to heterogeneous dissolution involving an increase of roughness at the micro-scale. Discrepancies between hydraulic apertures measured experimentally and calculated are also reported. The dissolution rate of the fracture walls is a bit fluctuant but globally decreases, which can be related to heterogeneous dissolution of the calcite grains at the surface and changes of the transport mechanisms close to the fluid–mineral interface.

The flow simulations show that the velocity profiles predicted by solving Navier–Stokes equations are noticeably different from the ideal parabolic profiles defined by the cubic law. Nevertheless, as already shown by Dijk and Berkowitz (1998), the effect on the macroscopic equivalent permeability seems negligible as deviation from the cubic law (a_m/a_{h-NS}) remains quite constant while the dissolution reaction progressed. Nonetheless, the presence of clays affects reactive transport within the fracture, despite their impact being of a much lower amplitude compared to a similar experiment at a lower flow rate (Noiriel et al., 2007a) or at the same flow rate but with a larger clay fraction within the sample (Noiriel et al., 2007b). Distortion of the velocity profiles as micro-roughness increases certainly has a great impact on transport of the reactants and products toward and away from the fracture surface, especially at the high Pe values (Cardenas et al., 2009) of the experiment. Although difficult to assess without a fully 3D modelling approach of transport in the fracture, the presence of areas of stagnant fluid (i.e. fracture wall surface overlaps) surely contributes to the fluctuant dissolution rate at sample-scale.

Although experimental acquisition and application of large data sets in numerical simulations are still challenging, we believe that X-ray micro-tomography coupled with experiments and modelling significantly increases our ability to determine the dominant local mechanisms that control the macroscopic properties, and therefore is advantageous for constraining upscaling procedures, especially when the evolution of the rock geometry is strongly dependant on the mineral spatial heterogeneity and arrangement.

Acknowledgments

This project was partially supported by the European Synchrotron Radiation Facility under Project ME-572. ESRF-ID19 staff is thanked for its helpful assistance during XMT scanning. Dr. Philip Boyle is gratefully acknowledged for his very careful reading of the paper.

Appendix A. Flow considerations into fractures

Single-phase flow of an incompressible fluid through a rock fracture is governed by the equations for conservation of mass

and momentum, i.e. the Navier–Stokes equations (Batchelor, 1967):

$$\begin{cases} \nabla \cdot \mathbf{u} = 0 \\ \rho(\mathbf{u} \cdot \nabla) \mathbf{u} = -\nabla P + \mu \nabla^2 \mathbf{u} + \mathbf{F} \end{cases} \quad (\text{A.1})$$

where \mathbf{u} is the velocity vector (m s^{-1}), ρ is the fluid density (kg m^{-3}), P is the reduced pressure ($\text{kg m}^{-1} \text{s}^{-2}$), μ is the viscosity ($\text{kg m}^{-1} \text{s}^{-1}$), and \mathbf{F} denotes the body forces applied to the fluid per unit volume ($\text{kg m}^{-2} \text{s}^{-2}$), which are generally limited to gravity. Stokes equations are obtained assuming that inertial forces are negligible, i.e. $\mathbf{u} \cdot \nabla \mathbf{u} \approx 0$ in Eq. (A.1). This first simplification is of interest for decreasing computational cost because it eliminates the strong non-linearity of the Navier–Stokes equation system. By definition, inertial effects decrease with \mathbf{u} , so that the better Stokes approximations are obtained at lower Reynolds numbers, Re , which is the usually the case in most hydrology cases. When a fracture is bounded by smooth and parallel walls, the Stokes equations can be solved exactly, which leads to the cubic law (e.g. Zimmerman and Yeo, 2000):

$$Q = \frac{a_h^3 l}{12\mu} \nabla P \quad (\text{A.2})$$

where a_h is the hydraulic aperture (m), which is accessible through hydraulic tests, Q is the volumetric flow rate ($\text{m}^3 \text{s}^{-1}$), l is the fracture width (m), and ∇P is the pressure gradient ($\nabla P = \Delta P/L$, with ΔP the differential pressure between the fracture inlet and outlet ($\text{kg m}^{-1} \text{s}^{-2}$), and L the fracture length (m)). When the cubic law is valid, hydraulic (a_h) and mechanical (a_m) apertures are by definition equal. But for real, rough-walled fractures, deviation from the cubic law is expected. Fracture roughness, aperture and surface correlation, tortuosity and contact areas have been pointed out as the main parameters controlling flow and transport in fractures (Adler and Thovert, 1999; Tsang, 1984; Witherspoon et al., 1980; Zimmerman and Yeo, 2000). One objective of these studies was to assess the validity of simplification of the Stokes equations into the Reynolds lubrication equation (Nicholl et al., 1999; Zimmerman and Yeo, 2000):

$$\nabla \cdot \left(\frac{a^3(y, z)}{12\mu} \nabla P \right) = 0 \quad (\text{A.3})$$

The Reynolds equations can be derived from the Navier–Stokes equations under certain geometrical and kinematic conditions, namely low velocity (i.e. low Reynolds numbers) and slow changes of the aperture geometry ($\|\nabla a\| \ll 0$), assuming that viscous forces are reduced to shear forces at the fracture wall interface ($\nabla^2 \mathbf{u} \approx \partial^2 \mathbf{u} / \partial z^2$) and superimposing a no-slip condition at the fracture wall interface ($\mathbf{u}|_{z\pm} = 0$). In that case, it is assumed that flux components perpendicular to the fracture plane are negligible, so that the local transmissivity is given by the cubic law for flow between parallel plates:

$$q = -\frac{a^3(y, z)}{12\mu} \nabla P \quad (\text{A.4})$$

where q is the local flux ($\text{m}^3 \text{s}^{-1}$). The so-called local cubic law (LCL) assumption is however also inadequate when fracture wall roughness (Brown, 1987) or normal stress (Glover et al., 1998; Raven and Gale, 1985) is too high. The domain of validity of the LCL is generally determined as the function of a limited set of macroscopic statistical variables of the fracture aperture, i.e. the mean $\langle a \rangle$ the standard deviation σ_a , and the correlation length λ_a . Inoue and Sugita (2003) showed that high order σ_a and λ_a approximation is required to capture the effect of anisotropic aperture distribution. Conversely, Brush and Thomson (2003), when comparing Navier–Stokes and LCL simulations for several synthetic fractures with various values of the relative roughness $\sigma_a/\langle a \rangle$ and of the roughness

slope $\langle a \rangle/\lambda_a$, showed that the LCL approach overestimates the flow rate at low Reynolds numbers ($Re < 100$) because both viscous shear stresses and inertial forces, which participate to head loss, were underestimated. Their better results were obtained with LCL approach using the geometric correction of the mechanical aperture proposed by Nicholl et al. (1999). For $Re < 1$ the flow rate discrepancies can be less than 10% if the relative roughness and the roughness slope are low (i.e. $\sigma_a/\langle a \rangle < 1$ and $\langle a \rangle/\lambda_a < 0.5$). Those values, which are closely similar to the results of Oron and Berkowitz (1998) and Zimmerman and Yeo (2000), are required mainly to minimise the inertial forces, but the effects of viscous forces may still be important for highly sloped fracture walls, producing skewed velocity profiles instead of the symmetric parabolic profiles imposed by the cubic law model (Tenchine and Gouze, 2005). Dijk et al. (1999), who explored the 3D velocity distribution in a natural rough-walled fracture using nuclear magnetic resonance imaging, also observed clusters of asymmetric velocity profiles in the vicinity of sharp discontinuities of the wall elevation. Nevertheless, it seems that the effect on volumetric flow rate and on the macroscopic equivalent permeability was negligible.

Appendix B. Reactive transport considerations into fractures

Transport of solutes in a fracture is described by the following macroscopic equation:

$$\partial_t C = \mathbf{D} \nabla^2 C - \mathbf{u} \nabla C + R(C) \quad (\text{B.1})$$

where C is the concentration of the species, \mathbf{u} is the velocity vector (the components of which are u_x , u_y and u_z), \mathbf{D} is the hydrodynamic dispersion tensor and $R(C)$ is the geochemical source term proportional to the reaction rate. Hydrodynamic dispersion involves Taylor and geometrical dispersion, and molecular diffusion.

In a fracture, solute transport is mainly controlled by the chemical reaction rate and the heterogeneity in the flow velocity. Positive feedback between flow regime and geochemical alteration can also occur, leading to instabilities and localisation of the dissolution. The usual parameters used for characterising these phenomena at the macro-scale are the Péclet number (Pe), the Damköhler number (Da), and the aperture variability, expressed as the ratio between the aperture standard deviation and its mean ($\sigma_a/\langle a \rangle$) (Cheung and Rajaram, 2002; Dijk and Berkowitz, 1998; Hanna and Rajaram, 1998; O'Brien et al., 2003; Szymczak and Ladd, 2004; Verberg and Ladd, 2002). Three-dimensional modelling of smooth fracture dissolution as a function of the Pe and Da was proposed by Szymczak and Ladd (2004). Their results fitted well with the experimental results obtained by Detwiler et al. (2003) on potassium-dihydrogen-phosphate (KDP) artificial fractures. The results of both those studies show a strong dependence of the dissolution pattern on Pe and Da. Low values of Da associated to high values of Pe appeared to favour large-scale homogeneous dissolution, whereas dominant channelling was observed at higher Da and intermediate Pe (Szymczak and Ladd, 2009).

References

- Adler, P.M., Thovert, J.F., 1999. Fracture and Fracture Networks. Springer, 489 pp.
- Batchelor, G.K., 1967. An Introduction to Fluid Dynamics. Cambridge University Press, 615 pp.
- Bertels, S.P., DiCarlo, D.A., 2001. Measurement of aperture distribution, capillary pressure, relative permeability, and in situ saturation in a rock fracture using computed tomography scanning. Water Resour. Res. 37 (3), 649–662.
- Bloomfield, J., 1996. Characterisation of hydrogeologically significant fracture distributions in the chalk: an example from the upper chalk of southern England. J. Hydrol. 184 (3–4), 355–379.
- Brown, S.R., 1987. Fluid flow through rock joints: the effect of surface roughness. J. Geophys. Res. 92(B2), 1337–1347.
- Brown, S.R., Scholz, C.H., 1985. Broad bandwidth study of the topography of natural rock surfaces. J. Geophys. Res. 90, 12575–12582.

- Brush, D.J., Thomson, N.R., 2003. Fluid flow in synthetic rough-walled fractures: Navier–Stokes, Stokes, and local cubic law simulations. *Water Resour. Res.* 39(4), 5–1–5–15.
- Cardenas, M.B., Slottke, D.T., Ketcham, R.A., Sharp Jr., J.M., 2009. Effects of inertia and directionality on flow and transport in a rough asymmetric fracture. *J. Geophys. Res. B: Solid Earth* 114, B06204. <http://dx.doi.org/10.1029/2009JB006336>.
- Cheung, W., Rajaram, H., 2002. Dissolution finger growth in variable aperture fractures: role of the tip-region flow field. *Geophys. Res. Lett.* 29 (22), 2075. <http://dx.doi.org/10.1029/2002GL015196>.
- Detwiler, R.L., 2008. Experimental observations of deformation caused by mineral dissolution in variable-aperture fractures. *J. Geophys. Res. B: Solid Earth* 113(B8), B08202. <http://dx.doi.org/10.1029/2008JB005697>.
- Detwiler, R.L., Glass, R.J., Bourcier, W.L., 2003. Experimental observation of fracture dissolution: the role of Peclet number on evolving aperture variability. *Geophys. Res. Lett.* 30 (12), 1648. <http://dx.doi.org/10.1029/2003GL017396>.
- Dijk, P., Berkowitz, B., 1998. Precipitation and dissolution of reactive solutes in fractures. *Water Resour. Res.* 34 (3), 457–470.
- Dijk, P., Berkowitz, B., Bendel, P., 1999. Investigation of flow in water-saturated rock fractures using nuclear magnetic resonance imaging (NMRI). *Water Resour. Res.* 35 (2), 347–360.
- Dijk, P., Berkowitz, B., Yechieli, Y., 2002. Measurement and analysis of dissolution patterns in rock fractures. *Water Resour. Res.* 38(2), 5–1–5–12.
- Ellis, B. et al., 2011. Deterioration of a fractured carbonate caprock exposed to CO₂-acidified brine flow. *Greenhouse Gas Sci. Technol.* 1 (3), 248–260.
- Enzmann, F., Kersten, M., Kienzer, B., 2004. Microscale Modelling of Fluid Transport in Fractured Granite Using a Lattice Boltzmann Method with X-ray Computed Tomography Data. LBNL Report 54275, Berkeley, CA, USA, pp. 300–304.
- Fredrich, J.T., Digiiovanni, A.A., Noble, D.R., 2006. Predicting macroscopic transport properties using microscopic image data. *J. Geophys. Res. B: Solid Earth* 111(B3), B03201. <http://dx.doi.org/10.1029/2005JB003774>.
- Glover, P.W.J., Matsuki, K., Hikima, R., Hayashi, K., 1998. Fluid flow in rough fractures and application to the Hachimantai geothermal hot dry rock test site. *J. Geophys. Res.* 103(B5), 9621–9635.
- Gonzales, R.C., Woods, R.E., 1992. *Digital Image Processing*. Addison-Wesley Publishing Company, Reading, Massachusetts, 716 pp.
- Gouze, P., Noiriél, C., Bruderer, C., Loggia, D., Leprovost, R., 2003. X-ray tomography characterisation of fracture surfaces during dissolution. *Geophys. Res. Lett.* 30 (5), 1267. <http://dx.doi.org/10.1029/2002/GL016755>.
- Hakami, E., Larsson, E., 1996. Aperture measurements and flow experiments on a single natural fracture. *Int. J. Rock Mech. Min. Sci. Geotech. Abstr.* 33(4), 395–404.
- Hanna, R.B., Rajaram, H., 1998. Influence of aperture variability on dissolutional growth of fissures in karst formation. *Water Resour. Res.* 11, 2843–2853.
- Herman, G.T., 1980. *Image Reconstruction from Projections: Fundamentals of Computerized Tomography*. Academic Press, New York, 316 pp.
- Inoue, J., Sugita, H., 2003. Fourth-order approximation of fluid flow through rough-walled rock fracture. *Water Resour. Res.* 39 (8), 1202. <http://dx.doi.org/10.1029/2002wr001411>.
- Karpyn, Z.T., Grader, A.S., Halleck, P.M., 2007. Visualization of fluid occupancy in a rough fracture using micro-tomography. *J. Colloid Interface Sci.* 307 (1), 181–187.
- Keller, A., 1998. High resolution, non-destructive measurement and characterisation of fracture apertures. *Int. J. Rock Mech. Min. Sci.* 35 (8), 1037–1050.
- Ketcham, R.A., Iturrino, G.J., 2005. Nondestructive high resolution visualization and measurement of anisotropic effective porosity in complex lithologies using high-resolution X-ray computed tomography. *J. Hydrol.* 302, 92–106.
- Koyama, T., Neretnieks, I., Jing, L., 2008. A numerical study on differences in using Navier–Stokes and Reynolds equations for modeling the fluid flow and particle transport in single rock fractures with shear. *Int. J. Rock Mech. Min. Sci.* 45 (7), 1082–1101.
- Kumar, A.T.A., Majors, P., Rossen, W., 1997. Measurement of aperture and multiphase flow in fractures with NMR imaging. *SPE Form. Eval.* 12 (2), 101–107.
- Landis, E.N., Nagy, E.N., Keane, D.T., 2003. Microstructure and fracture in three dimensions. *Eng. Fract. Mech.* 70, 911–925.
- Méheust, Y., Schmittbuhl, J., 2001. Geometrical heterogeneities and permeability anisotropy of rough fractures. *J. Geophys. Res.* 106(B2), 2089–2102.
- Myers, N.O., 1962. Characterization of surface roughness. *Wear* 5, 182–189.
- Nicholl, M.J., Rajaram, H., Glass, R.J., Detwiler, R.L., 1999. Saturated flow in a single fracture: evaluation of the Reynolds equation in measured aperture field. *Water Resour. Res.* 35 (11), 3361–3373.
- Nikolaïdis, N., Pitas, I., 2001. *3-D Image Processing Algorithms*. John Wiley & Sons Inc., New York, 176 pp.
- Noiriél, C., Gouze, P., Bernard, D., 2004. Investigation of porosity and permeability effects from microstructure changes during limestone dissolution. *Geophys. Res. Lett.* 31 (24), L24603. <http://dx.doi.org/10.1029/2004GL021572>.
- Noiriél, C., Gouze, P., Madé, B., 2007a. Time-resolved 3D characterisation of flow and dissolution patterns in a single rough-walled fracture. In: Krasny, J., Sharp, J. (Eds.), *IAH Selected Papers Series 9 on Groundwater in Fractured Rocks*. Taylor & Francis, pp. 629–642.
- Noiriél, C., Madé, B., Gouze, P., 2007b. Impact of coating development on the hydraulic and transport properties in argillaceous limestone fracture. *Water Resour. Res.* 43, W09046. <http://dx.doi.org/10.1029/2006WR005379>.
- Noiriél, C., Luquot, L., Madé, B., Raimbault, L., Gouze, P., van der Lee, J., 2009. Changes in reactive surface area during limestone dissolution: an experimental and modelling study. *Chem. Geol.* 265 (1–2), 160–170.
- Noiriél, C., Steefel, C.I., Yang, L., Ajo-Franklin, J., 2012. Upscaling calcium carbonate precipitation rates from pore to continuum scale. *Chem. Geol.* 318–319, 60–74.
- O'Brien, G.S., Bean, C.J., McDermott, F., 2003. Numerical investigations of passive and reactive flow through generic single fracture with heterogeneous permeability. *Earth Planet. Sci. Lett.* 213, 271–284.
- Oh, W., Lindquist, W.B., 1999. Image thresholding by indicator kriging. *IEEE Trans. Pattern Anal. Mach. Intell.* 21 (7), 590–602.
- Oron, A.P., Berkowitz, B., 1998. Flow in rock fractures: the local cubic law assumption reexamined. *Water Resour. Res.* 34 (11), 2811–2825.
- Ortoleva, P., Merino, E., Moore, C., Chadam, J., 1987. Geochemical self-organization I. Reaction – transport feedbacks and modeling approach. *Am. J. Sci.* 287, 979–1007.
- Patir, N., Cheng, H.S., 1978. An average flow model for determining effects of the three-dimensional roughness on partial hydrodynamic lubrication. *J. Lubr. Technol.* 100, 12–17.
- Pitas, I., 2000. *Digital Image Processing Algorithms and Applications*. Wiley, 432 pp.
- Plummer, L.N., Wigley, T.M.L., Parkhurst, D.L., 1978. The kinetics of calcite dissolution in CO₂–water systems at 5°C to 60°C and 0.0 to 1.0 atm CO₂. *Am. J. Sci.* 278, 179–216.
- Raven, K.G., Gale, J.E., 1985. Water flow in natural rock fracture as a function of stress and sample size. *Int. J. Rock Mech. Min. Sci. Geotech. Abstr.* 22(4), 251–161.
- Schmittbuhl, J., Schmitt, F., Scholz, C., 1995. Scaling invariance of crack surfaces. *J. Geophys. Res.* 100(B4), 5953–5973.
- Sheppard, A.P., Sok, R.M., Averdunk, H., 2004. Techniques for image enhancement and segmentation of tomographic images of porous materials. *Physica A* 339, 145–151.
- Steefel, C.I., Lasaga, A.C., 1990. Evolution of dissolution patterns: permeability change due to coupled flow and reaction. In: Melchior, D., Bassett, R.L. (Eds.), *Chemical Modeling of Aqueous Systems II*. American Chemical Society, Washington, DC, pp. 212–225.
- Sugano, K., 2008. Theoretical comparison of hydrodynamic diffusion layer models used for dissolution simulation in drug discovery and development. *Int. J. Pharm.* 363 (1–2), 73–77.
- Szymczak, P., Ladd, A.C.J., 2004. Microscopic simulations of fracture dissolution. *Geophys. Res. Lett.* 31, L23606. <http://dx.doi.org/10.1029/2004GL021297>.
- Szymczak, P., Ladd, A.C.J., 2009. Wormhole formation in dissolving fractures. *J. Geophys. Res. B: Solid Earth* 114, B06203. <http://dx.doi.org/10.1029/2008JB006122>.
- Tenchine, S., Gouze, P., 2005. Density contrast effects on tracer dispersion in variable aperture fractures. *Adv. Water Resour.* 28, 273–289.
- Tsang, Y.W., 1984. The effect of tortuosity on fluid flow through a single fracture. *Water Resour. Res.* 20 (9), 1209–1215.
- van der Lee, J., Lomench, C., 2004. Towards a common thermodynamic database for speciation models. *Radiochim. Acta* 92, 811–818.
- Vandersteen, K., Busselen, B., Van den Abeele, K., Carmeleir, J., 2003. Quantitative characterization of fracture apertures using microfocus computed tomography. In: Mees, F., Swennen, R., Van Geet, M., Jacobs, P. (Eds.), *Applications of X-ray Computed Tomography in the Geosciences*. Geol. Soc. Spec. Publ. 215, 243 pp, pp. 61–69.
- Verberg, R., Ladd, A.C.J., 2002. Simulation of chemical erosion in rough fracture. *Phys. Rev. E: Stat. Nonlinear Soft Matter Phys.* 65 (056311).
- Walters, D.A., Wong, R.C.K., Kantzas, A., 1998. The application of computed-assisted tomography in the analysis of fracture geometry. *Geotech. Test. J.* 21 (4), 328–335.
- Witherspoon, P.A., Wang, J.S.Y., Iwai, K., Gale, J.E., 1980. Validity of cubic law for fluid flow in a deformable rock fracture. *Water Resour. Res.* 16 (6), 1016–1024.
- Zimmerman, R.W., Bodvarsson, G.S., 1996. Hydraulic conductivity of rock fractures. *Transp. Porous Media* 23, 1–30.
- Zimmerman, R.W., Yeo, I., 2000. Fluid flow in rock fractures: from the Navier–Stokes equations to the cubic law. In: Faybishenko, B., Witherspoon, P.A., Benson, S.M. (Eds.), *Dynamics of Fluids in Fractured Rocks*. Geophysical Monograph 122, pp. 213–224.
- Zimmerman, R.W., Kumar, S., Bodvarsson, G.S., 1991. Lubrication theory analysis of the permeability of rough-walled fractures. *Int. J. Rock Mech. Min. Sci. Geotech. Abstr.* 28(4), 325–331.